RSC Applied Interfaces

ROYAL SOCIETY OF CHEMISTRY

PAPER

View Article Online
View Journal | View Issue

Cite this: *RSC Appl. Interfaces*, 2025, **2**, 167

Salicylaldimine-functionalized L-phenylalanine-based pseudopeptides: zinc-instructed conformational tuning of self-assembled nanostructures†

Kamlesh Kumar Nigam, Surabhi Asthana and Mrituanjay D. Pandey *

Received 12th July 2024,
Accepted 17th October 2024

DOI: 10.1039/d4lf00251b

rsc.li/RSCApplInter

Pseudopeptidic bioinspired materials are emerging soft matter for recognizing biologically relevant species, supramolecular self-assembled nanostructures, and advanced nanoscience applications. Therefore, we have developed a novel C_2-symmetric pseudopeptide using L-phenylalanine amino acid and salicylaldehyde with varying aliphatic spacers. Pseudopeptides show a high selectivity toward Zn(II) ion with significant fluorescence enhancement. The self-assembly exhibits a random spherical nanostructure morphology transformed into a densely packed spherical microstructure morphology after incubating Zn(II) ions through conformational tuning. This zinc-guided rearrangement of self-assembly and interaction with BSA proteins holds significant potential for applications in nanobioscience.

Introduction

Nature employs molecular self-assembly to construct new functional structures using several fundamental components, including nucleic acids, amino acids, peptides, and phospholipids.[1–3] Notably, peptide self-assembly has garnered significant attention due to its importance in biology and soft matter.[3–5] In metalloproteins, amino acids influence coordination chemistry as amino acid side chains and backbone heteroatoms provide the bulk of ligands to coordinate with metal ions.[6] Many researchers are devoted to synthesizing a system constructed from amino acids and non-natural moieties to facilitate coordination with various metal ions. In this context, pseudopeptides are modified peptides containing amino acid building blocks[7] that can coordinate with metal ions and exhibit diverse applications in sensing and catalysis.[8–11] Various pseudopeptidic ligands have been reported to undergo complexation with active metal ions relevant to many biochemical events.[12]

Detecting heavy metal ions received significant attention in the food industry and environmental sectors due to their potential hazard to human health and the ecosystem.[13] Among various metal ions, zinc is the second most abundant transition metal in humans after iron. It plays a very significant role in various biological processes, including enzyme regulation, gene expression, functioning as a physical co-factor in metalloproteins, and neural signal transmission[14–16] Moderate levels of Zn(II) ions are essential for all living organisms; however, an excessive concentration of Zn(II) ions in the human body is responsible for neurodegenerative syndromes.[17] Conversely, deficiency of Zn(II) ion has been implicated in several diseases, including neurological disorders, growth retardation, immune deficiency, Parkinson's disease, cerebral ischemia, epilepsy, and Alzheimer's disease.[18–20] Zn(II) ion also causes environmental pollution due to its extensive use in the electroplating industry.[21,22] Therefore, there is a need to develop fluorescence sensors for selective and sensitive recognition of Zn(II) ions under physiological conditions.

Various Zn(II) ion detection analysis methods have been developed, including electrochemical method,[23] colorimetric method,[24] voltammetry,[25] flame atomic absorption spectrometry,[26] inductively coupled plasma-optical emission spectrometry *etc.*[27] However, these methods have certain limitations, including high cost, lengthy procedures, complex operational requirements, the need for professional technical expertise, and susceptibility to interference of other elements.[28,29] In contrast, the fluorescence detection method has attracted many researchers due to its fast response, cost-effectiveness, high sensitivity, simplicity, and compatibility with biological systems.[30–33] Hence, fluorescence sensors have been extensively used for biological detection, environmental monitoring, imaging, diagnosis of diseases, and other applications.[34] Various fluorescence sensors for the selective recognition of Zn(II) ions have been synthesized using different

Department of Chemistry, Institute of Science, Banaras Hindu University, Varanasi-221005, India. E-mail: mdpandey.chem@bhu.ac.in

† Electronic supplementary information (ESI) available. See DOI: https://doi.org/10.1039/d4lf00251b

fluorophore moieties.[35–41] Nevertheless, these sensors exhibit drawbacks, such as interference issues, high costs, and poor solubility. Hence, a highly selective and sensitive sensor is needed to recognize Zn(II) ions. In this regard, Schiff bases are extensively explored for sensing purposes due to their excellent ability to coordinate with various metal ions.[42–47]

Sustainable development goals motivated us to synthesize and characterize the novel pseudopeptides **1–3** for selective and sensitive detection of zinc(II) under physiological conditions. Recently, our group has developed such C_2-symmetric pseudopeptides for sensing applications.[48–50] Compounds **1–3** are formed by the condensation of L-phenylalanine-derived pseudopeptides connected with a series of aliphatic linkers (ethylenediamine, 1,4-diaminobutane, and 1,6-diaminohexane) and salicylaldehyde (Scheme 1). AFM study reveals that neat **1–3** exhibit a spherical shape nanostructure morphology with different average particle sizes, whereas incubating with Zn(II) ion causes a significant change in the self-assembly pattern and shows a densely packed spherical shape microstructure morphology with conformational tuning.

Experimental

Synthesis of 1 (2*S*,2′*S*)-*N*,*N*′-(ethane-1,2-diyl)bis(2-(((*E*)-2-hydroxybenzylidene)amino)-3-phenylpropanamide)

Compounds **A–C** were prepared using previous literature procedures.[51] **A** (708 mg) was dissolved in 25 ml of dry ethanol, forming a clear pale yellow transparent solution, followed by dropwise addition of 20 ml of a dry ethanolic solution of salicylaldehyde (2-hydroxybenzaldehyde) (488 mg, 4 mmol) at 90 °C. The reaction mixture was refluxed for 4–5 h, evaporating the solvent under reduced pressure. The crude product was washed with 10 ml *n*-hexane several times to obtain product **1**. Yield (0.810 g, 1.43 mmol, 72%); m.p. 145 °C; IR (KBr pellet): 3431, 3329, 3062, 3029, 2919, 2886, 1628, 1651 cm^{-1}; ^1H NMR (500 MHz, $CDCl_3$) δ 12.28 (s, 2H), 7.84 (s, 2H), 7.30 (t, J = 8.0 Hz, 2H), 7.23–7.10 (m, 12H), 7.04 (d, J = 8.0 Hz, 2H), 6.95 (d, J = 8.0 Hz, 2H), 6.83 (t, J = 8.0 Hz, 2H), 6.56 (s, 2H), 3.98 (dd, J = 9.5, 4.0 Hz, 2H), 3.37–3.34 (m, 4H), 3.04 (dd, J = 14.5, 9.0 Hz, 2H); $^{13}C\{^1H\}$ NMR (126 MHz, $CDCl_3$) δ 172.08, 167.82, 160.62, 137.18, 133.31, 132.26, 129.88, 128.53, 126.94, 119.30, 118.50, 117.18, 75.65, 40.94, 39.99; HRMS (ESI-TOF) m/z: $[M + H]^+$ calcd for $C_{34}H_{34}N_4O_4$, 563.2653; found, 563.2630.

Synthesis of 2 (2*S*,2′*S*)-*N*,*N*′-(butane-1,4-diyl)bis(2-(((*E*)-2-hydroxybenzylidene)amino)-3-phenylpropanamide)

Compound **2** was synthesized as described above, starting from **B** (765 mg, 2 mmol) and salicylaldehyde (488 mg, 4 mmol). Yield (0.874 g, 1.47 mmol, 74%); m.p. 160 °C; IR (KBr pellet): 3428, 3359, 3062, 3029, 2945, 2880, 1651, 1628 cm^{-1}; ^1H NMR (500 MHz, $CDCl_3$) δ 12.36 (s, 2H), 7.90 (s, 2H), 7.32 (t, J = 8.0 Hz, 2H), 7.22–7.08 (m, 12H), 6.95 (d, J = 8.0 Hz, 2H), 6.86–6.83 (m, 2H), 6.14 (s, 2H), 4.01 (dd, J = 8.0, 4.0 Hz, 2H), 3.37 (dd, J = 13.5, 4.0 Hz, 2H), 3.28–3.12 (m, 4H), 3.08 (dd, J = 13.0, 8.0 Hz, 2H), 1.41 (s, 4H); $^{13}C\{^1H\}$ NMR (126 MHz, $CDCl_3$) δ 170.79, 167.73, 160.58, 137.11, 133.34, 132.25, 129.90, 128.57, 126.90, 119.39, 118.83, 117.14, 75.50, 41.02, 39.08, 26.82; HRMS (ESI-TOF) m/z: $[M + H]^+$ calcd for $C_{36}H_{38}N_4O_4$, 591.2966; found, 591.2946.

Synthesis of 3 (2*S*,2′*S*)-*N*,*N*′-(hexane-1,6-diyl)bis(2-(((*E*)-2-hydroxybenzylidene)amino)-3-phenylpropanamide)

Compound **3** was synthesized as described above, starting from **C** (821 mg, 2 mmol) and salicylaldehyde (488 mg, 4 mmol). Yield (0.903 g, 1.45 mmol, 73%); m.p. 138 °C; IR (KBr pellet): 3437, 3352, 3062, 3030, 2938, 2852, 1654, 1628 cm^{-1}; ^1H NMR (500 MHz, $CDCl_3$) δ 12.42 (s, 2H), 7.86 (s, 2H), 7.31 (t, J = 8.0 Hz, 2H), 7.21–7.05 (m, 12H), 6.94 (d, J = 9.5 Hz, 2H), 6.86–6.83 (m, 2H), 6.12 (s, 2H), 4.00 (dd, J = 9.0, 4.0 Hz, 2H), 3.39 (dd, J = 13.5, 4.0 Hz, 2H), 3.28–3.16 (m, 4H), 3.08 (dd, J = 13.0, 9.0 Hz, 2H), 1.44–1.34 (m, 4H), 1.21 (s, 4H); $^{13}C\{^1H\}$ NMR (126 MHz, $CDCl_3$) δ 170.78, 167.56, 160.59, 137.13, 133.29, 132.24, 129.90, 128.56, 126.92, 119.37, 118.48, 117.10, 75.56, 41.09, 39.25, 29.38, 26.29; HRMS (ESI-TOF) m/z: $[M + H]^+$ calcd for $C_{38}H_{42}N_4O_4$, 619.3279; found, 619.3294.

Results and discussion

Compounds **1–3**, constructed from L-phenylalanine by introducing a series of aliphatic central spacers (ethylenediamine, 1,4-diaminobutane, and hexamethylenediamine), could be developed by condensation of salicylaldehyde with **A–C**.

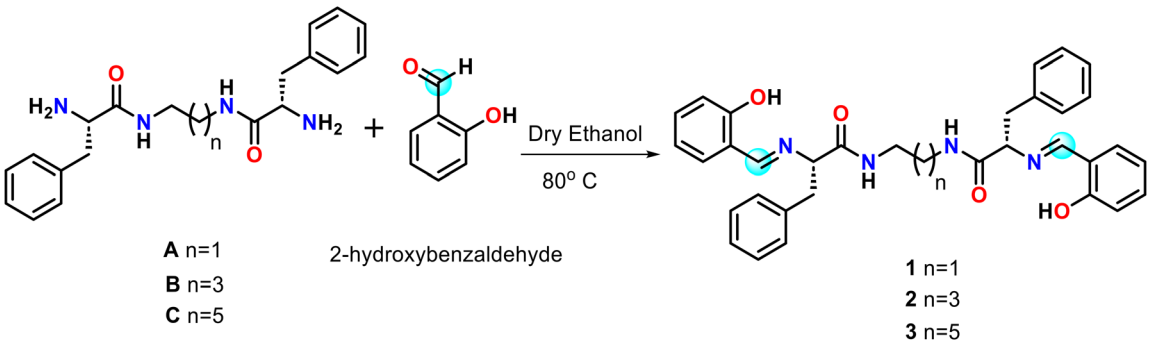

Scheme 1 Synthetic route of peptidomimetics **1–3**.

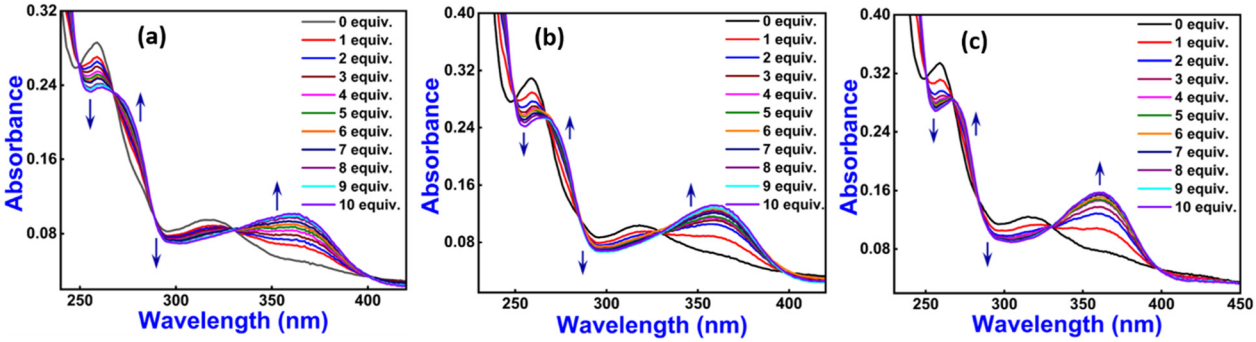

Fig. 1 Absorption titration spectra of **1** (a), **2** (b) and **3** (c) with Zn(II) (0 to 10 equiv.) ions in HEPES buffer (ethanol : water = 3 : 7 v/v, pH ~7.4, 10 μM, at r.t.).

Compounds **1–3** show folding properties due to the presence of an aliphatic central spacer by which they can easily interact with numerous metal ions and play a crucial role in metal sensing (Scheme 1). Compounds **1–3** were characterized by spectroscopic techniques including ^{1}H NMR, ^{13}C NMR, FTIR, and mass spectroscopy (Fig. S1–S9†).

The neat **1–3** give two absorption bands at 259 and 315 nm attributed to intraligand $\pi \rightarrow \pi^*$ and $n \rightarrow \pi^*$ transition[52] and display a considerable change on the addition of Zn(II) ion. In contrast, other metal ions do not show any significant change (Fig. S10†). Absorption titration experiment was performed by successive addition of Zn(II) ion (0 to 10 equiv.) to **1–3** (10 μM), and we have found distinct isosbestic points centered at approximately 398 nm, 330 nm, 284 nm, 267 nm, and 250 nm (Fig. 1).

The neat **1–3** reveal one weak fluorescence emission band at approximately 432 nm on excitation at 315 nm. To investigate the unique sensing ability of **1–3** with different analytes, we tested various metal ions, including Ag(I), Ca(II), Cd(II), Co(II), Cu(II), Fe(III), Hg(II), K(I), Na(I), Ni(II), Pb(II), and Zn(II) (counter anion is NO_3^-) and found that only Zn(II) ions give significant fluorescence enhancement (~74%, ~74% and ~81%, respectively) (Fig. 2).

To further elucidate the coordination ability of **1–3** with Zn(II) ion, fluorescence titration experiments were performed *via* increasing the concentration of Zn(II) ion (0 to10 equiv.), and we observed a promising outcome, in which the emission intensity of neat **1–3** dramatically changed with 'turn-on' mode at 432 nm with minor red shifting (approximately 20 nm) (Fig. 3). In this study, we have calculated the fluorescence quantum yield (ϕ) by applying quinine sulfate monohydrate (QS, ϕ = 0.54 in 0.5 M sulfuric acid) as a standard for neat **1–3** and found its values to be ϕ = 0.31, 0.24 and 0.20, respectively, whereas **1**–Zn(II), **2**–Zn(II) and **3**–Zn(II) show fluorescence quantum yield values of ϕ = 0.91, 0.62 and 0.33, respectively[53] (Table S1†). The increased quantum yield value supports the fluorescence enhancement phenomenon of **1–3** with Zn(II) ion. Furthermore, we have evaluated the average fluorescence lifetime decay for neat **1–3** and was found to be 1.284 ns, 0.609 ns, and 1.084 ns, respectively, whereas on adding Zn(II) ion, we observed an increase in average fluorescence lifetime decay values for **1**–Zn(II), **2**–Zn(II), and **3**–Zn(II) of 1.835 ns, 3.218 ns, and 1.390 ns, respectively. This result further supports the fluorescence enhancement of **1–3** with Zn(II) ion (Fig. S11 and Table S2†).

The above results of fluorescence enhancement directed us to perform a colorimetric experiment using **1–3** with several metal ions. Therefore, to investigate the colorimetric change, we added various metal ions (10 mM) (Ag(I), Ca(II), Cd(II), Co(II), Cu(II), Fe(III), Hg(II), K(I), Na(I), Ni(II), Pb(II), and Zn(II)) (counter anion is NO_3^-) to **1–3** (10 μM) and observed that only Zn(II) ions give a significant luminescence under UV

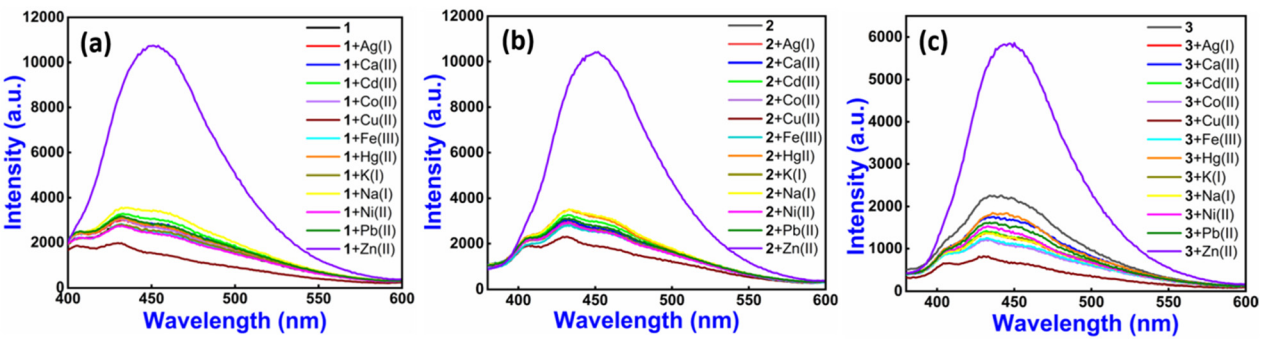

Fig. 2 Emission spectra of **1** (a), **2** (b) and **3** (c) with various metal ions (10 mM) in HEPES buffer (ethanol : water = 3 : 7 v/v, pH ~7.4, 10 μM, at r.t.) (λ_{ex} = 315 nm for **1–3**).

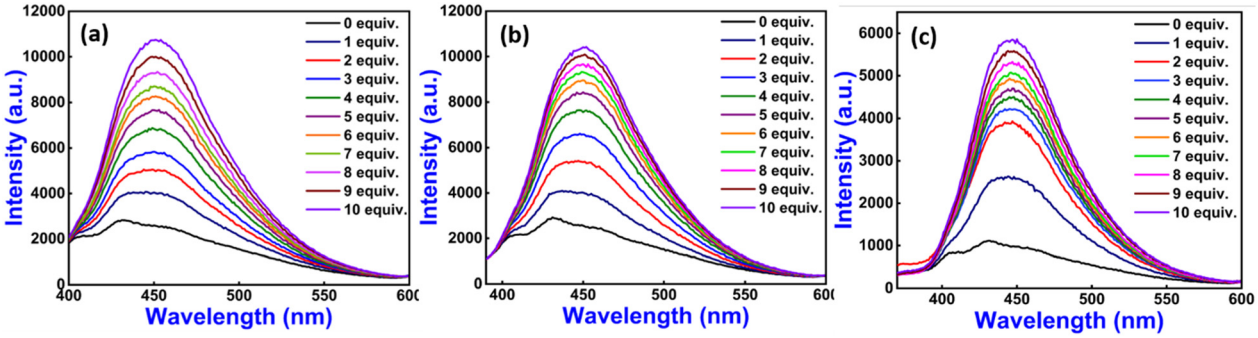

Fig. 3 Emission titration spectra of **1** (a), **2** (b), and **3** (c) with Zn(II) (0 to 10 equiv.) ions in HEPES buffer (ethanol : water = 3 : 7 v/v, pH ~7.4, 10 μM, at r.t.) (λ_{ex} = 315 nm for **1**–**3**).

light (long-range UV 365 nm). The other experimental metal ions did not provide any considerable change (Fig. S12†).

On excitation, neat **1**–**3** exhibit very low fluorescence intensity due to electron transfer from imine nitrogen to the phenyl ring by photoinduced electron transfer (PET). On adding Zn(II) ions, they coordinate with **1**–**3** through imine nitrogen and the oxygen atom of the salicylaldehyde moiety; therefore the electron density on imine nitrogen reduces and no electron density is available on imine nitrogen for the PET process, leading to an increase in fluorescence intensity[54,55] (Fig. S13†). The ESIPT and C=N isomerization mechanism cannot be ruled out for fluorescence enhancement.[34d,56]

The reversibility study is an essential factor to satisfy the need for fluorescence sensors for reusability purposes. Here, we have tested the reversibility behavior of **1**–Zn(II), **2**–Zn(II), and **3**–Zn(II) with EDTA. The addition of EDTA (10 equiv.) to a solution of **1**–Zn(II), **2**–Zn(II), and **3**–Zn(II) revealed that **1**–**3** regenerate quickly and show fluorescence quenching, and further addition of Zn(II) ions (10 equiv.) in the same solution enhances the fluorescence intensity again (Fig. S14†). Hence, this result suggests the reversible nature of **1**–**3** for recognizing the Zn(II) ion. A proposed model of reversibility is shown in Fig. S15.†

To further investigate the high selectivity of **1**–**3** for Zn(II), an interference experiment was carried out by emission spectroscopy. On addition of Zn(II) ion (10 equiv.) to neat **1**–**3** (10 μM), the emission intensity was increased and this was followed by the addition of each competitive metal ion (10 equiv.) including Ag(I), Ca(II), Cd(II), Co(II), Cu(II), Fe(III), Hg(II), K(I), Na(I), Ni(II), and Pb(II); no variation occurred in emission intensity in the presence of other competitive metal ions. Hence, this result suggests that **1**–**3** seem to be highly selective for Zn(II) ion (Fig. S16†).

We performed a Job's plot experiment *via* emission data to investigate the binding stoichiometry of **1**–Zn(II), **2**–Zn(II), and **3**–Zn(II). This experiment suggests the 1 : 1 binding stoichiometry (Fig. S17†). Further, to verify the binding mode of **1** with Zn(II) (using zinc acetate), a HRMS experiment was performed for the **1**–Zn(II) complex. As shown in Fig. S18,† a peak appearing at m/z = 685.4379 (found), corresponding to $[\mathbf{1} + Zn + H + CH_3COOH]^+$ m/z = 685.2005 (calcd), was observed, suggesting the formation of the **1**–Zn(II) complex in a 1 : 1 ratio. For the binding constant (K_a) of **1**–**3** with Zn(II), we have used the 1 : 1 binding isotherm. The binding constant (K_a) was calculated by a graph between **1** and [Zn(II)] and found to be 1.26×10^5 M^{-1} for **1**–Zn(II), 1.66×10^5 M^{-1} for **2**–Zn(II) and 0.60×10^5 M^{-1} for **3**–Zn(II) system (Fig. S19†).

Varying concentrations of Zn(II) ion (10^{-2}–10^{-12} M) were added to the neat **1**–**3** (10 μM) to investigate the sensitivity with Zn(II) ion. A plot between the concentration of Zn(II) ion and emission intensity reveals a significant change at 10^{-6} M for the **1**–Zn(II) system, whereas at 10^{-7} M for both **2**–Zn(II) and **3**–Zn(II) systems (Fig. S20†). Zn(II) ion 10^{-6} M (1×10^{-6}–9×10^{-6} M) was added to **1** (10 μM), and the limit of detection (LOD) was calculated to be 8.30×10^{-6} M for the **1**–Zn(II) system. In a similar way, for better accuracy, 10^{-7} M (1×10^{-7}–9×10^{-7} M) Zn(II) ion solution was added to **2** and **3** (10 μM) and the estimated limit of detection (LOD) values were 8.28×10^{-7} M for **2**–Zn(II) and 8.34×10^{-7} M for **3**–Zn(II) by using the equation $3\sigma/S$, where σ indicates the standard deviation of blank **1**–**3** and S is the slope (Fig. S21†).[57] The LOD value is too low compared to some previously reported results by potential researchers (Table S3†). Hence, probes **1**–**3** can detect Zn(II) ions at physiological conditions; however, **2** and **3** probably have better detection capabilities because enough flexible linkers allows it to hold metal ions more efficiently.

The interaction between bovine serum albumin (BSA) and **1**–**3**–Zn(II) complexes was also investigated *via* emission spectra. Notably, the BSA sensor plays a crucial role in the study, as it helps to better understand the binding interactions and fluorescence response. Serum albumin in blood has multiple binding sites which can interact with drug molecules to form a stable protein–drug complex which could affect the absorption, distribution and activity of drugs, and BSA offers a high structural homology with human serum albumin.[58]

As described in the above sensing studies, **1**–**3** exhibit a significant fluorescence enhancement spectrum with Zn(II) ions. However, when introducing 1 equiv. (1600 μl) of a BSA solution (~20 μM) to the **1**–**3**–Zn(II) complexes (10 μM), a significant reduction in fluorescence intensity occurs without any

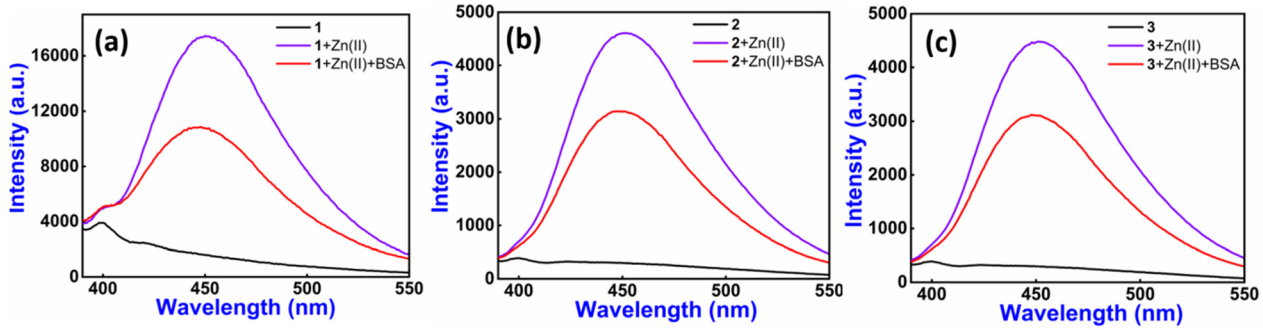

Fig. 4 Quenching spectra of the **1**–**3**–Zn(II) complexes with BSA: (a) **1**–Zn(II) complex, (b) **2**–Zn(II) complex and (c) **3**–Zn(II) complex in the presence of BSA (~20 μM) in HEPES buffer (ethanol : water = 3 : 7 v/v, pH ~7.4, 10 μM, at r.t.).

wavelength shift (38% for **1**–Zn(II), 32% for **2**–Zn(II), and 30% for **3**–Zn(II)) as depicted in Fig. 4. We have also performed emission titration experiment on the **1**–**3**–Zn(II) complexes with sequential addition (0 to 1 equiv.) of BSA (Fig. S22†). This investigation indicates that the BSA protein functions as a quencher in the presence of the **1**–**3**–Zn complex, suggesting its potential significance in the biomedical field, as it provides a real-time method to study protein interactions, functions as a biomarker and can also be employed in imaging of BSA distribution in cells or tissues.

Circular dichroism (CD) spectroscopy was performed to investigate the conformational change in **1**–**3** on adding Zn(II) ion (Fig. S23†). Neat **1**–**3** (10 μM) exhibit a mixed secondary structure with one major CD spectrum at 267 nm with a negative extremum. In addition to Zn(II) ion (10 equiv.), **1** shows two spectra at 247 nm and 271 nm with a negative extremum and one major spectrum centered at 215 nm with a positive extremum, whereas **2** and **3** reveal only two CD spectra at 270 nm (negative extremum) and 215 nm (positive extremum). This result suggests that the **1**–**3**–Zn(II) system shows a beta-sheet like secondary structure which is also supported by an FTIR deconvolution study (Fig. S30†). Furthermore, it is concluded that conformational change occurs in **1**–**3** on the addition of Zn(II) ion.[48,59]

The formation of secondary structures observed in the CD spectra motivated us to investigate the morphological behavior further. We employed AFM to complement the spectroscopic data with high-resolution imaging, providing a comprehensive picture of the molecular behavior and aggregation dynamics in response to metal ion coordination. This integrated approach allowed us to correlate the secondary structural transitions with the nanoscale surface morphology, offering more profound insights into the interaction mechanisms and conformational changes driven by Zn(II) ion binding. The AFM experiment explored the structural morphology of **1**–**3** through various possible self-assembly of molecules and investigated the change in self-assembly pattern by adding Zn(II) ions. We have observed that neat **1** exhibits a spherical shape nanostructure morphology with root mean square roughness (Rq) = 52.649 nm, average roughness (Ra) = 27.687 nm, and maximum profile peak height = 66.255 nm (Fig. 5(a)). The spherical shape morphology may be arising due to the self-aggregation of molecules *via* appropriate non-covalent interactions. The histogram plot shows the average particle size of 541 nm (Fig. 5(c)). Next, we checked the effect of Zn(II) ion on the structural morphology of **1**. Our observation revealed that 12 h of incubation of Zn(II) caused a significant change in the self-assembly of **1** and provided a large spherical shape nanostructure morphology with root mean square roughness (Rq) = 712 nm, average roughness (Ra) = 553 nm, and maximum profile peak height = 962 nm (Fig. 5(b)). The sizeable 3D self-assembled spherical shape microsphere morphology (in comparison to the nanosphere morphology of neat **1**) arises due to the aggregation of more **1**–Zn(II) units with appropriate non-covalent interactions.[48,59,60] The histogram plot shows an increased average particle size of 2048 nm after incubation of the Zn(II) ion, which supports more **1**–Zn(II) unit aggregates and forms a large spherical shape nanostructure morphology (Fig. 5(d)). The spherical shape morphology of both **1** and **1**–Zn(II) was also supported by the TEM image (Fig. S24†). A proposed model representation is also illustrated in Fig. 6 to understand the formation of more dense spherical morphology with large size microspheres of **1**–Zn(II) from the nanospherical structure of neat **1**.

Similarly, neat **2** also exhibits spherical shape nanostructure morphology with root mean square roughness (Rq) = 51.372 nm, average roughness (Ra) = 37.149 nm, and maximum profile peak height = 96.347 nm (Fig. S25(a)†). The histogram plot shows an average particle size of 805 nm (Fig. S25(c)†). On incubating Zn(II) ion (for 12 h) with **2**, we noticed a comparatively larger spherical shape nanostructure morphology for **2**–Zn(II) with root mean square roughness (Rq) = 546 nm, average roughness (Ra) = 427 nm, and maximum profile peak height = 474 nm (Fig. S25(b)†). The larger spherical shape nanostructure morphology arose due to the aggregation of more **2**–Zn(II) units with non-covalent interaction and 3D self-assembly. This result is supported by a histogram plot that exhibits an increase in average particle size of 1774 nm, implying the transformation of nanospheres (in neat **2**) to microspheres (Fig. S25(d)†). A proposed model represents the formation of a microsphere of **2**–Zn(II) from the nanospherical structure of neat **2** (Fig. S26†).

In this study, neat **3** also exhibits a spherical shape nanostructure morphology with root mean square roughness

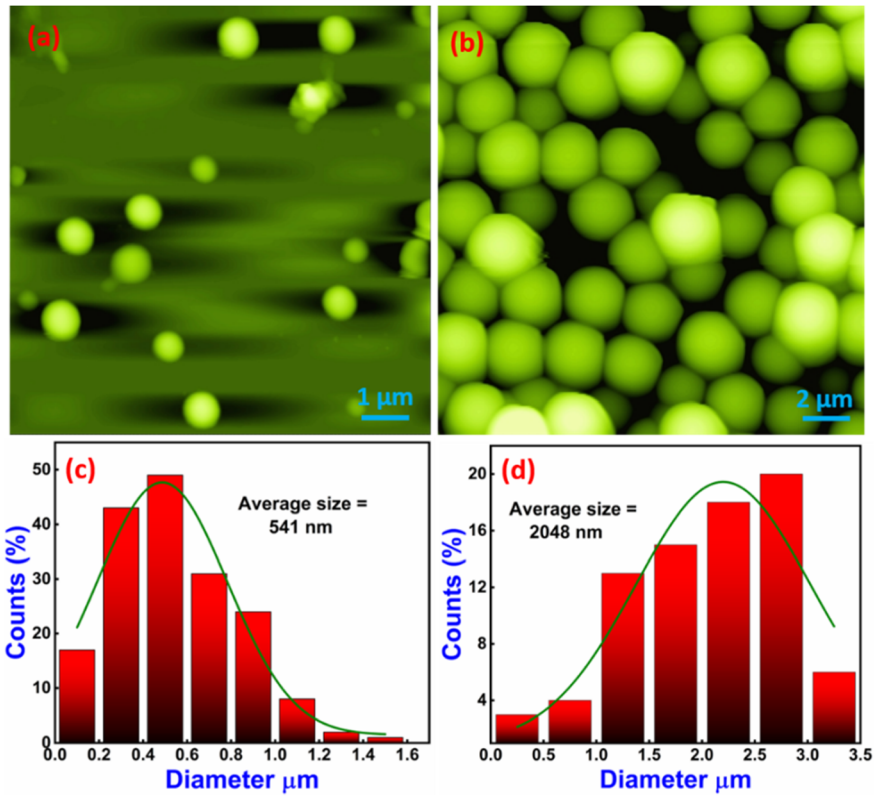

Fig. 5 (a) 2D AFM image of self-assembled structure for **1**, (c) its corresponding particle (spherical) size distribution histogram, (b) 2D AFM image of self-assembled structure for **1**–Zn(II) complex, (d) its corresponding particle (spherical) size distribution histogram.

(Rq) = 40.674 nm, average roughness (Ra) = 27.936 nm, and maximum profile peak height = 39.601 nm (Fig. S27(a)†). The histogram plot shows the average particle size of 750 nm (Fig. S27(c)†). On incubating Zn(II) ion (for 12 h) with **3**, a

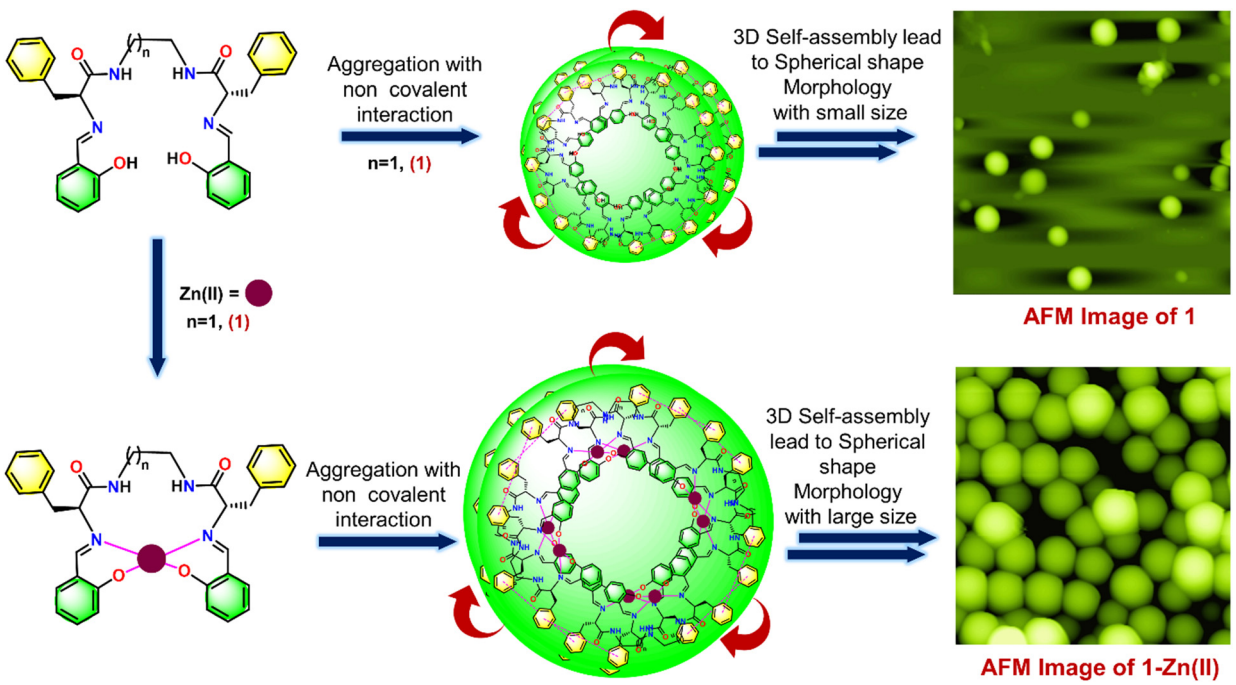

Fig. 6 Proposed model to represent the change in structural morphology of **1** by adding Zn(II) ions *via* 2D AFM image.

large size spherical shape nanostructure morphology was observed for **3**–Zn(II) with root mean square roughness (Rq) = 240.294 nm, average roughness (Ra) = 192.096 nm, and maximum profile peak height = 208 nm (Fig. S27(b)†). The sizable spherical shape nanostructure morphology arose due to the aggregation of many **3**–Zn(II) units with non-covalent interaction, leading to the formation of microspheres. This result is supported by a histogram plot in which we observed an increase in average particle size of 1063 nm (Fig. S27(d)†). A proposed model represents the formation of a microspherical morphology of **3**–Zn(II) from the nanospherical structure of neat **3** (Fig. S28†).

The above AFM study revealed that **1–3** show a spherical shape nanostructure morphology with different average particle sizes, whereas on incubation of Zn(II) ion, it reveals a densely packed spherical shape nanostructure morphology with different average particle sizes. Hence, we have concluded that the self-assembly pattern of bioinspired materials **1–3** significantly changed from nanospherical structure to microspherical structure *via* interaction with Zn(II) ion. Therefore, we find that the zinc-assisted, morphologically transformed, nanostructured L-phenylalanine-based pseudopeptides are promising materials for nanobioscience applications.[60]

We utilized dynamic light scattering (DLS) analysis to examine the size of **1–3** in the presence and absence of Zn(II) ions. Neat **1** and **2** exhibit particle size distribution centered at 420 nm and 1040 nm (diameter), respectively, whereas neat **3** shows at 267 nm and 5468 nm (Fig. S29(a–c)†). Adding 10 equiv. of Zn(II) ion to **1–3** (10 μM) gives a particle size distribution with different diameters at 660 nm and 5468 nm for **1**–Zn(II), 420 nm, and 5468 nm for **2**–Zn(II) and 420 nm and 4043 nm for **3**–Zn(II) (Fig. S29(d–f)†).

The formation of specific secondary structures depends on the skeleton of molecular building blocks that self-assemble and form well-defined stable structures.[61] Hence, Fourier-transform infrared (FTIR) spectroscopy was performed to investigate the structure of the compound. The amide region is used to explore the significant change in secondary structure contribution and amide backbone. It was observed that the amide region of **1–3** exhibits similar band participation, centered at 1627 and 1668 cm^{-1} for **1**, 1627, 1656 and 1668 cm^{-1} for **2**, and 1628 and 1654 cm^{-1} for **3**.

The IR deconvolution spectra in the amide region explore the quantitative analysis of secondary structure contributions in **1–3**. It was observed that **1** shows α-helix 0%, β-sheet 61%, random coil 0%, and antiparallel β-sheet 16% conformation in secondary structural contribution (Fig. 7(a) and (d)). In the same way, **2** exhibits secondary structural contribution, α-helix 0%, β-sheet 50%, random coil 0%, and antiparallel β-sheet 30% conformation (Fig. 7(b) and (e)). In this sequence, compound **3** shows α-helix 0%, β-sheet 30%, random coil 0%, and antiparallel β-sheet 46% conformation (Fig. 7(c) and (f)).

On adding Zn(II) ion to **1–3**, we have observed that the **1**–Zn(II) complex shows α-helix 0%, β-sheet 50%, random coil 22%, and antiparallel β-sheet 25%, the **2**–Zn(II) complex shows α-helix 0%, β-sheet 30%, random coil 25%, and antiparallel β-sheet 22%, whereas the **3**–Zn(II) complex

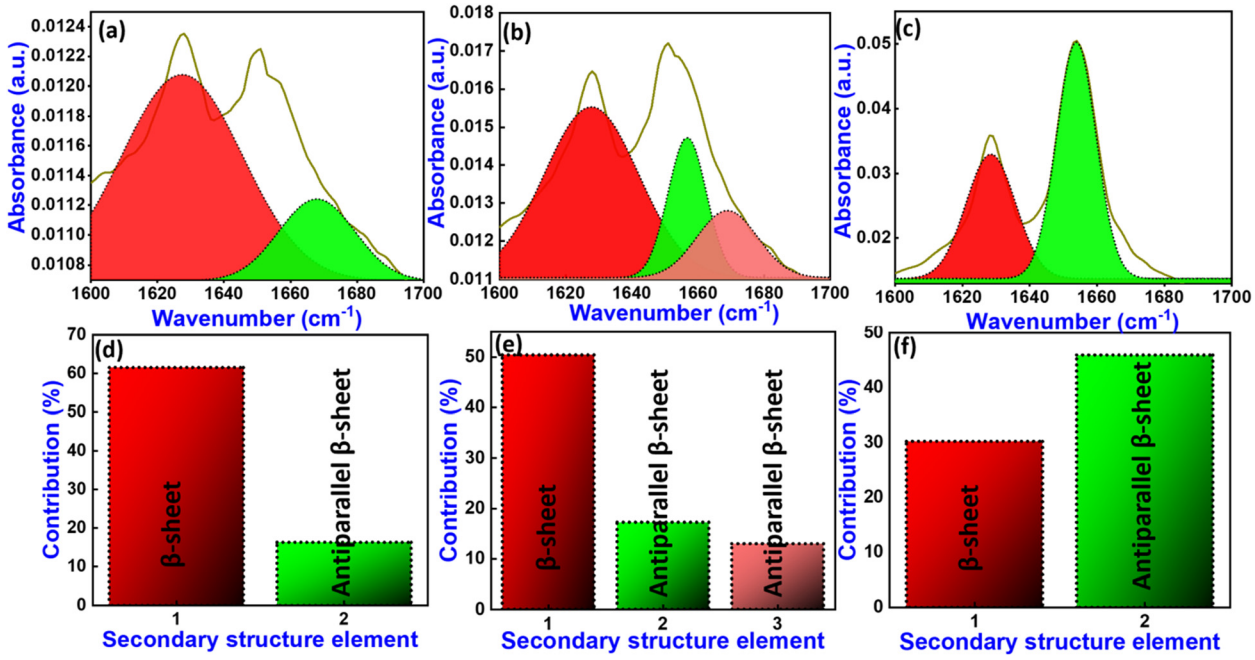

Fig. 7 (a) The FTIR spectrum of **1** (solid brown line) and its deconvolution (dashed colored area). (d) Secondary structure contributions of **1** in self-assembly. (b) The FTIR spectrum of **2** (solid brown line) and its deconvolution (dashed colored area). (e) Secondary structure contributions of **2** in self-assembly. (c) The FTIR spectrum of **3** (solid brown line) and its deconvolution (dashed colored area). (f) Secondary structure contributions of **3** in self-assembly. Fitting of deconvolution plot by multiple Gaussian peaks in the amide region ranging from 1610 to 1680 cm^{-1}.

displays α-helix 0%, β-sheet 75%, random coil 7%, and antiparallel β-sheet 25% conformation in secondary structural contribution (Fig. S30†).

Density functional theory (DFT) calculations were performed to examine the binding mode of Zn(II) with compounds **1–3** and to determine the relative energies of the highest occupied molecular orbital (HOMO) and the lowest unoccupied molecular orbital (LUMO) for both **1–3** and the **1–3**–Zn(II) complexes. The B3LYP (6-31g(d′,p′)) and B3LYP/LANL2DZ basis sets are used to theoretically optimize the ground-state geometry of **1–3** and **1–3**–Zn(II) complexes, respectively (Fig. S31†).

The energy gap between the HOMO and the LUMO for compound **1** is determined to be 4.67 eV, while for the **1**–Zn(II) complex it is found to be 3.70 eV. The reduction in this energy gap by 0.97 eV from compound **1** to the **1**–Zn(II) complex strongly implies the formation of a stable **1**–Zn(II) complex, as depicted in Fig. 8. In a similar way, compounds **2** and **3** also formed stable complexes with Zn(II) ion, investigated by DFT study (Fig. S32 and S33†).

The absorption characteristics of compounds **1–3** are critical for their applications in different arenas. Experimental techniques such as UV-vis spectroscopy provide direct absorbance measurements, while computational verification offers insights into the electronic transitions responsible for these spectral features. This study employs time-dependent density functional theory (TD-DFT) to compute the electronic excitation energies and compare them with the experimentally observed absorbance spectra. The ground-state geometry of **1–3** was optimized using DFT with the B3LYP functional and the LANL2DZ basis set. Excited-state properties were subsequently calculated using TD-DFT to obtain the electronic transition energies. The oscillator strengths for each transition were calculated to predict the absorbance spectrum. All calculations were performed using the Gaussian 16 software package.

The computed absorption spectrum of **1**–Zn(II) shows key electronic transitions at 321.01 nm. These agree with the experimental absorbance peaks observed at 315 nm. The slight shift in the computed spectrum can be attributed to solvent interactions and phase differences. Nevertheless, the overall agreement between experimental and theoretical spectra confirms the validity of TD-DFT for modeling the optical properties of **1**. The electron density in the HOMO lies on the linker moiety, and that in the LUMO shifts to the zinc atom of the complex. Similarly, the computed absorption spectra of compound **3**–Zn(II) show electronic transition at 315.49 nm, which agrees with the experimental absorbance observed at 315 nm (Fig. S34†).

The computational verification of the absorbance spectrum of compounds **1** and **3** using TD-DFT shows strong agreement with experimental data, confirming the reliability of this method for predicting optical properties. The predicted transitions provide detailed insights into the electronic structure, which may be helpful for future applications in drug design and nanoscience fields.

We have reported C_2-symmetry pseudopeptides **1–3**, which revealed high selectivity and sensitivity with Zn(II) ion *via* fluorescence 'turn-on' mode through PET mechanism. The Job's plot experiment reveals 1 : 1 stoichiometry between **1–3** and Zn(II), further supported by DFT calculation. The binding constant (K_a) for **1**–Zn(II), **2**–Zn(II), and **3**–Zn(II) was calculated to be 1.16 × 10^4 M^{-1}, 1.25 × 10^4 M^{-1} and 5.0 ×

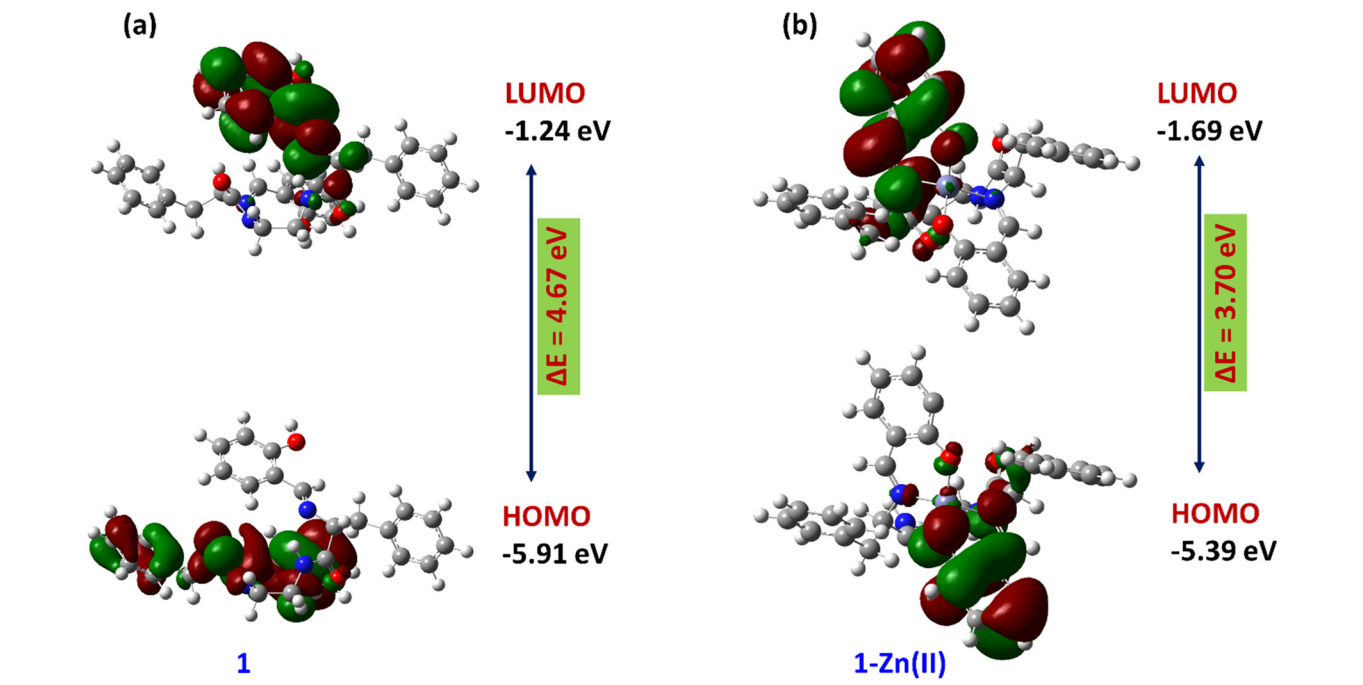

Fig. 8 Optimized energy level and energy gap between the HOMO and LUMO of **1** (a) and the **1**–Zn(II) complex (b).

10^4 M^{-1}, respectively. On increasing the length of the aliphatic spacer, we obtained the best result for detection limit values which were found to be 8.30×10^{-6} M for **1**–Zn(II), 8.28×10^{-7} M for **2**–Zn(II), and 8.34×10^{-7} M for **3**–Zn(II). The BSA protein is a quencher for metal-mediated pseudopeptides, suggesting its potential significance in the biomedical field. The self-assembly of neat **1–3** exhibits a spherical shape nanostructure morphology with different average particle sizes, but on incubating with Zn(II) ion the self-assembly pattern of **1–3** revealed a refined densely packed spherical shape microstructure morphology with different average particle sizes. The dynamic light scattering (DLS) spectra analyzed the particle size distribution. CD spectra revealed its metal-mediated conformational tuning. The Zn-mediated pseudopeptides show great biological relevance due to their cheap, sustainable, and biocompatible nature. Hence, the next-generation soft bioinspired materials look forward to being useful for peptide-based nanobioscience applications.

Data availability

The data supporting this article have been included as part of the ESI.†

Conflicts of interest

The authors declare that there are no interpersonal or financial conflicts.

Acknowledgements

The authors acknowledge the Institute of Eminence (IoE)-Banaras Hindu University for financial support. KKN and SA are thankful to UGC-CSIR for a fellowship. MDP acknowledges the CST Government of UP (Project ID-3382) for the funding.

References

1 (*a*) D. Pochan and O. Scherman, Introduction: Molecular Self-Assembly, *Chem. Rev.*, 2021, **121**, 13699–13700, DOI: **10.1021/acs.chemrev.1c00884**; (*b*) S.-H. Yu, R. O'Reilly, L. Jiang and N. A. Kotov, The New Era of Self-Assembled Nanomaterials, *Acc. Chem. Res.*, 2022, **55**, 1783–1784, DOI: **10.1021/acs.accounts.2c00327**.

2 F. Sheehan, D. Sementa, A. Jain, M. Kumar, M. Tayarani-Najjaran, D. Kroiss and R. V. Ulijn, Peptide-Based Supramolecular Systems Chemistry, *Chem. Rev.*, 2021, **121**, 13869–13914, DOI: **10.1021/acs.chemrev.1c00089**.

3 (*a*) C. Ménard-Moyon, V. Venkatesh, K. V. Krishna, F. Bonachera, S. Verma and A. Bianco, Self-Assembly of Tyrosine into Controlled Supramolecular Nanostructures, *Chem. - Eur. J.*, 2015, **21**, 11681–11686, DOI: **10.1002/chem.201502076**; (*b*) Y. Huo, J. Hu, Y. Yin, P. Liu, K. Cai and W. Ji, Self-Assembling Peptide-Based Functional Biomaterials, *ChemBioChem*, 2023, **24**, e202200582, DOI: **10.1002/cbic.202200582**.

4 (*a*) S. V. Luis and I. Alfonso, Bioinspired Chemistry Based on Minimalistic Pseudopeptides, *Acc. Chem. Res.*, 2014, **47**, 112–124, DOI: **10.1021/ar400085p**; (*b*) I. Alfonso, From simplicity to complex systems with bioinspired pseudopeptides, *Chem. Commun.*, 2016, **52**, 239–250, DOI: **10.1039/C5CC07596C**.

5 V. Haridas, Tailoring of Peptide Vesicles: A Bottom-Up Chemical Approach, *Acc. Chem. Res.*, 2021, **54**, 1934–1949, DOI: **10.1021/acs.accounts.0c00690**.

6 S. Blasco, M. I. Burguete, M. P. Clares, E. García-España, J. Escorihuela and S. V. Luis, Coordination of Cu^{2+} Ions to C_2 Symmetric Pseudopeptides Derived from Valine, *Inorg. Chem.*, 2010, **49**, 7841–7852, DOI: **10.1021/ic100748g**.

7 I. Avan, C. D. Hall and A. R. Katritzky, Peptidomimetics via Modifications of Amino Acids and Peptide Bonds, *Chem. Soc. Rev.*, 2014, **43**, 3575, DOI: **10.1039/C3CS60384A**.

8 A. Mohan, A. Koh, G. Gate, A. Calkins, K. McComas and A. Fuller, Solid-Phase Synthesis of Azole-Comprising Peptidomimetics and Coordination of a Designed Analog to Zn^{2+}, *Molecules*, 2018, **23**, 1035, DOI: **10.3390/molecules23051035**.

9 M. D. Pandey, V. Martí-Centelles, M. I. Burguete, N. Montoya, S. V. Luis, E. García-España and A. Doménech-Carbó, Bisferrocenyl-Functionalized Pseudopeptides: Access to Separated Ionic and Electronic Contributions for Electrochemical Anion Sensing, *RSC Adv.*, 2016, **6**, 35257–35266, DOI: **10.1039/C6RA04482D**.

10 F. Esteve, B. Altava, M. I. Burguete, M. Bolte, E. García-Verdugo and S. V. Luis, Pseudopeptidic Macrocycles as Cooperative Minimalistic Synzyme Systems for the Remarkable Activation and Conversion of CO_2 in the Presence of the Chloride Anion, *Green Chem.*, 2020, **22**, 4697–4705, DOI: **10.1039/D0GC01449D**.

11 M. I. A. Ibrahim, X. Solimando, L. Stefan, G. Pickaert, J. Babin, C. Arnal-Herault, D. Roizard, A. Jonquières, J. Bodiguel and M.-C. Averlant-Petit, A Lysine-Based 2:1-[α/Aza]-Pseudopeptide Series Used as Additives in Polymeric Membranes for CO_2 Capture: Synthesis, Structural Studies, and Application, *RSC Adv.*, 2023, **13**, 10051–10067, DOI: **10.1039/D3RA00409K**.

12 (*a*) L. Gorla, V. Martí-Centelles, B. Altava, M. I. Burguete and S. V. Luis, Cu^{2+} recognition by N, N′-benzylated bis (amino amides), *Dalton Trans.*, 2017, **46**(8), 2660–2669, DOI: **10.1039/C6DT04756D**; (*b*) L. Gorla, V. Marti-Centelles, L. Freimuth, B. Altava, M. I. Burguete and S. V. Luis, Cu^{2+}, Zn^{2+}, and Ni^{2+} Complexes of C2-Symmetric Pseudopeptides with an Aromatic Central Spacer, *Inorg. Chem.*, 2016, **55**(15), 7617–7629, DOI: **10.1021/acs.inorgchem.6b01066**; (*c*) V. Martí-Centelles, D. K. Kumar, A. J. White, S. V. Luis and R. Vilar, Zinc(II) coordination polymers with pseudopeptidic ligands, *CrystEngComm*, 2011, **13**(23), 6997–7008, DOI: **10.1039/C1CE05872J**.

13 Z. Chen, Z. Zhang, J. Qi, J. You, J. Ma and L. Chen, Colorimetric Detection of Heavy Metal Ions with Various Chromogenic Materials: Strategies and Applications, *J. Hazard. Mater.*, 2023, **441**, 129889, DOI: **10.1016/j.jhazmat.2022.129889**.

14 (*a*) W. Cao, X.-J. Zheng, J.-P. Sun, W.-T. Wong, D.-C. Fang, J.-X. Zhang and L.-P. Jin, A Highly Selective Chemosensor for

Al(III) and Zn(II) and Its Coordination with Metal Ions, *Inorg. Chem.*, 2014, **53**, 3012–3021, DOI: **10.1021/ic402811x**; (*b*) Z. Xu, J. Yoon and D. R. Spring, Fluorescent Chemosensors for Zn^{2+}, *Chem. Soc. Rev.*, 2010, **39**, 1996, DOI: **10.1039/B916287A**.

15 H. Liu, Y. Dong, B. Zhang, F. Liu, C. Tan, Y. Tan and Y. Jiang, An Efficient Quinoline-Based Fluorescence Sensor for Zinc(II) and Its Application in Live-Cell Imaging, *Sens. Actuators, B*, 2016, **234**, 616–624, DOI: **10.1016/j.snb.2016.04.175**.

16 H. Haase and L. Rink, Multiple Impacts of Zinc on Immune Function, *Metallomics*, 2014, **6**, 1175, DOI: **10.1039/c3mt00353a**.

17 C. J. Frederickson, J.-Y. Koh and A. I. Bush, The Neurobiology of Zinc in Health and Disease, *Nat. Rev. Neurosci.*, 2005, **6**, 449–462, DOI: **10.1038/nrn1671**.

18 P. Wang, Q. Wang, Z. Guo, S. Xue, B. Chen, Y. Liu, W. Ren, X. Yang and S. Wen, A Bifunctional Peptide-Based Fluorescent Probe for Ratiometric and "Turn-on" Detection of Zn(II) Ions and Its Application in Living Cells, *Spectrochim. Acta, Part A*, 2022, **268**, 120653, DOI: **10.1016/j.saa.2021.120653**.

19 R. Wulandari, A. Ardiansyah, H. Setiyanto and V. Saraswaty, A Novel Non-Enzymatic Electrochemical Uric Acid Sensing Method Based on Nanohydroxyapatite from Eggshell Biowaste Immobilized on a Zinc Oxide Nanoparticle Modified Activated Carbon Electrode (Hap-Esb/ZnONPs/ACE), *RSC Adv.*, 2023, **13**, 12654–12662, DOI: **10.1039/D3RA01214J**.

20 L. Yan, C. Zhou, J. Li, H. Yang, X. Wu and L. Li, A Near-Infrared Fluorescent Probe Based on Dicyanisophorone for the Detection of Zinc Ions (Zn^{2+}) in Water and Living Cells, *J. Fluoresc.*, 2023, **33**, 201–207, DOI: **10.1007/s10895-022-03040-y**.

21 Q. Lin, T.-T. Lu, X. Zhu, T.-B. Wei, H. Li and Y.-M. Zhang, Rationally Introduce Multi-Competitive Binding Interactions in Supramolecular Gels: A Simple and Efficient Approach to Develop Multi-Analyte Sensor Array, *Chem. Sci.*, 2016, **7**, 5341–5346, DOI: **10.1039/C6SC00955G**.

22 J. M. Berg and Y. Shi, The Galvanization of Biology: A Growing Appreciation for the Roles of Zinc, *Science*, 1996, **271**, 1081–1085, DOI: **10.1126/science.271.5252.1081**.

23 R. Gulaboski, V. Mireski and F. Scholz, An Electrochemical Method for Determination of the Standard Gibbs Energy of Anion Transfer between Water and N-Octanol, *Electrochem. Commun.*, 2002, **4**, 277–283, DOI: **10.1016/S1388-2481(02)00264-3**.

24 M. K. Song, N. F. Adham and H. Rinderknecht, A Simple, Highly Sensitive Colorimetric Method for the Determination of Zinc in Serum, *Am. J. Clin. Pathol.*, 1976, **65**, 229–233, DOI: **10.1093/ajcp/65.2.229**.

25 F. Torma, M. Kádár, K. Tóth and E. Tatár, Nafion®/2,2′-Bipyridyl-Modified Bismuth Film Electrode for Anodic Stripping Voltammetry, *Anal. Chim. Acta*, 2008, **619**, 173–182, DOI: **10.1016/j.aca.2008.05.004**.

26 J. Chen and K. C. Teo, Determination of Cadmium, Copper, Lead and Zinc in Water Samples by Flame Atomic Absorption Spectrometry after Cloud Point Extraction, *Anal. Chim. Acta*, 2001, **450**, 215–222, DOI: **10.1016/S0003-2670(01)01367-8**.

27 A. Rajabi Khorrami, A. R. Fakhari, M. Shamsipur and H. Naeimi, Pre-Concentration of Ultra Trace Amounts of Copper, Zinc, Cobalt and Nickel in Environmental Water Samples Using Modified C18 Extraction Disks and Determination by Inductively Coupled Plasma–Optical Emission Spectrometry, *Int. J. Environ. Anal. Chem.*, 2009, **89**, 319–329, DOI: **10.1080/03067310802549953**.

28 L. Gu, S. Yang, B. Miao, Z. Gu, J. Wang, W. Sun, D. Wu and J. Li, Electrical Detection of Trace Zinc Ions with an Extended Gate-AlGaN/GaN High Electron Mobility Sensor, *Analyst*, 2019, **144**, 663–668, DOI: **10.1039/C8AN01770K**.

29 X. Mu, L. Shi, L. Yan and N. Tang, A 2-Hydroxy-1-Naphthaldehyde Schiff Base for Turn-on Fluorescence Detection of Zn^{2+} Based on PET Mechanism, *J. Fluoresc.*, 2021, **31**, 971–979, DOI: **10.1007/s10895-021-02732-1**.

30 E. P. S. Pratt, L. J. Damon, K. J. Anson and A. E. Palmer, Tools and Techniques for Illuminating the Cell Biology of Zinc, *Biochim. Biophys. Acta, Mol. Cell Res.*, 2021, **1868**, 118865, DOI: **10.1016/j.bbamcr.2020.118865**.

31 K. P. Carter, A. M. Young and A. E. Palmer, Fluorescent Sensors for Measuring Metal Ions in Living Systems, *Chem. Rev.*, 2014, **114**, 4564–4601, DOI: **10.1021/cr400546e**.

32 C. J. Fahrni, D. Bourassa and R. Dikdan, Probing Biological Trace Metals with Fluorescent Indicators, in *Metals in the Brain*, ed. A. White, Neuromethods, Humana Press, New York, NY, 2017, vol. 124, pp. 71–107, DOI: **10.1007/978-1-4939-6918-0_5**.

33 L. Zhu, Z. Yuan, J. T. Simmons and K. Sreenath, Zn(ii)-coordination modulated ligand photophysical processes – the development of fluorescent indicators for imaging biological Zn(ii) ions, *RSC Adv.*, 2014, **4**, 20398–20440, DOI: **10.1039/C4RA00354C**.

34 (*a*) A. C. Sedgwick, L. Wu, H.-H. Han, S. D. Bull, X.-P. He, T. D. James, J. L. Sessler, B. Z. Tang, H. Tian and J. Yoon, Excited-state intramolecular proton-transfer (ESIPT) based fluorescence sensors and imaging agents, *Chem. Soc. Rev.*, 2018, **47**, 8842–8880, DOI: **10.1039/C8CS00185E**; (*b*) T. Maddeshiya, M. K. Jaiswal, A. Tamrakar, G. Mishra, C. Awasthi and M. D. Pandey, Pyrene Appendant Triazole-based Chemosensors for Sensing Applications, *Curr. Org. Synth.*, 2024, **21**, 421–435, DOI: **10.2174/1570179420666230621124119**; (*c*) A. Srivastava, G. Mishra, A. K. Pathak, S. Pandey, C. Awasthi, M. D. Pandey and K. Behera, Pyrene-Appended Luminescent Probes for Selective Detection of Toxic Heavy Metals and Live Cell Applications, *ChemistrySelect*, 2024, **9**, e202303914, DOI: **10.1002/slct.202303914**; (*d*) M. D. Pandey, A. Tamrakar, M. A. Wani, G. Mishra, A. Srivastava and R. Pandey, Advancements in the Development of Fluorescent Chemosensors Based on C=N Bond Isomerization/Modulation Mechanistic Approach, *Anal. Methods*, 2024, **16**, 2198–2228, DOI: **10.1039/D3AY02321D**; (*e*) M. D. Pandey, S. Asthana, M. V. Mouli, A. Tamrakar, M. A. Wani, A. K. Mishra and R. Pandey, Recent Advances in AIEgen-based Chemosensors for Small Molecule Detection, with a Focus on Ion Sensing, *Anal. Methods*, 2024, **16**, 4431–4484, DOI: **10.1039/D4AY00618F**.

35 (*a*) Y. Li, R. Song, J. Zhao, Y. Liu and J. Zhao, Synthesis, Structure, and Properties of a Novel Naphthalene-Derived Fluorescent Probe for the Detection of Zn2+, *Polyhedron*,

2023, **234**, 116336, DOI: 10.1016/j.poly.2023.116336; (*b*) V. K. Gupta, A. K. Singh, L. K. Kumawat and N. Mergu, An Easily Accessible Switch-on Optical Chemosensor for the Detection of Noxious Metal Ions Ni(II), Zn(II), Fe(III) and UO2(II), *Sens. Actuators, B*, 2016, **222**, 468–482, DOI: 10.1016/j.snb.2015.08.063; (*c*) S. Asthana, T. Maddeshiya, A. Tamrakar, P. Kumar, N. Garg and M. D. Pandey, l-Tryptophan-based pyrene conjugate for intracellular zinc-guided excimer emission and controlled nano-assembly, *Anal. Methods*, 2024, **16**, 5633–5641, DOI: 10.1039/D4AY00979G.

36 J. Sun, Z. Liu, Y. Wang, S. Xiao, M. Pei, X. Zhao and G. Zhang, A Fluorescence Chemosensor Based on Imidazo[1,2-a]Quinoline for Al^{3+} and Zn^{2+} in Respective Solutions, *RSC Adv.*, 2015, **5**, 100873–100878, DOI: 10.1039/C5RA21055K.

37 M. Patil, K. Keshav, M. K. Kumawat, S. Bothra, S. K. Sahoo, R. Srivastava, J. Rajput, R. Bendre and A. Kuwar, Monoterpenoid Derivative Based Ratiometric Fluorescent Chemosensor for Bioimaging and Intracellular Detection of Zn^{2+} and Mg^{2+} Ions, *J. Photochem. Photobiol., A*, 2018, **364**, 758–763, DOI: 10.1016/j.jphotochem.2018.07.015.

38 J. Gong, Y. Li, C. Zhang, J. Huang and Q. Sun, A Thiazolo[4,5-b]Pyridine-Based FLuorescent Probe for Detection of Zinc Ions and Application for in Vitro and in Vivo Bioimaging, *Talanta*, 2018, **185**, 396–404, DOI: 10.1016/j.talanta.2018.03.061.

39 S. Chakraborty, S. Lohar, K. Dhara, R. Ghosh, S. Dam, E. Zangrando and P. Chattopadhyay, A New Half-Condensed Schiff Base Platform: Structures and Sensing of Zn^{2+} and $H_2PO_4^-$ Ions in an Aqueous Medium, *Dalton Trans.*, 2020, **49**, 8991–9001, DOI: 10.1039/D0DT01594F.

40 H. Liu, T. Liu, J. Li, Y. Zhang, J. Li, J. Song, J. Qu and W.-Y. Wong, A Simple Schiff Base as Dual-Responsive Fluorescent Sensor for Bioimaging Recognition of Zn^{2+} and Al^{3+} in Living Cells, *J. Mater. Chem. B*, 2018, **6**, 5435–5442, DOI: 10.1039/C8TB01743C.

41 Y. Wang, Z.-G. Wang, X.-Q. Song, Q. Chen, H. Tian, C.-Z. Xie, Q.-Z. Li and J.-Y. Xu, A Dual Functional Turn-on Non-Toxic Chemosensor for Highly Selective and Sensitive Visual Detection of Mg^{2+} and Zn^{2+} : The Solvent-Controlled Recognition Effect and Bio-Imaging Application, *Analyst*, 2019, **144**, 4024–4032, DOI: 10.1039/C9AN00583H.

42 V. Inbaraj and D. Udhayakumari, A Review on Schiff Base as Colorimetric and Fluorescence Sensors for D-Metal Ions, *Curr. Chem. Lett.*, 2023, **12**, 739–758, DOI: 10.5267/j.ccl.2023.5.001.

43 T. J. Dathees, S. P. Makarios Paul, A. Sanmugam, A. Abiram, S. Murugan, R. S. Kumar, A. I. Almansour, N. Arumugam, R. Nandhakumar and D. Vikraman, Naphthalene derived Schiff base as a reversible fluorogenic chemosensor for aluminium ions detection, *Spectrochim. Acta, Part A*, 2024, **308**, 123732, DOI: 10.1016/j.saa.2023.123732.

44 K. Rout, A. K. Manna, M. Sahu, J. Mondal, S. K. Singh and G. K. Patra, Triazole-based novel bis Schiff base colorimetric and fluorescent turn-on dual chemosensor for Cu^{2+} and Pb^{2+}: application to living cell imaging and molecular logic gates, *RSC Adv.*, 2019, **9**, 25919–25931, DOI: 10.1039/C9RA03341F.

45 S. M. Basheer, P. Rasin, V. Manakkadan, V. P. V. Palakkeezhillam and A. Sreekanth, Recent Advancements in Schiff Base Fluorescence Chemosensors for the Detection of Heavy Metal Ions, *IntechOpen*, 2023, DOI: 10.5772/intechopen.109022.

46 S. Khan, X. Chen, A. Almahri, E. S. Allehyani, F. A. Alhumaydhi, M. M. Ibrahim and S. Ali, Recent developments in fluorescent and colorimetric chemosensors based on schiff bases for metallic cations detection: A review, *J. Environ. Chem. Eng.*, 2021, **9**, 106381, DOI: 10.1016/j.jece.2021.106381.

47 N. Kumari, S. Singh, M. Baral and B. K. Kanungo, Schiff Bases: A Versatile Fluorescence Probe in Sensing Cations, *J. Fluoresc.*, 2023, **33**, 859–893, DOI: 10.1007/s10895-022-03135-6.

48 (*a*) K. K. Nigam, A. Tamrakar and M. D. Pandey, l-Phenylalanine-Derived Pseudopeptidic Bioinspired Materials: Zn(II) Induced Fluorescence Enhancement and Precise Tuning of Self-Assembled Nanostructures, *Soft Matter*, 2023, **19**, 7266–7270, DOI: 10.1039/D3SM00703K; (*b*) K. K. Nigam and M. D. Pandey, Zinc-Induced Luminescent l-Valine-Based Pseudopeptidic Soft Bioinspired Materials for Precise Tuning of Nanoassembly, *ACS Biomater. Sci. Eng.*, 2024, **10**, 1393–1402, DOI: 10.1021/acsbiomaterials.3c01954.

49 A. Tamrakar, K. K. Nigam and M. D. Pandey, Copper-Guided Tuning of Supramolecular Nano-Assembly in Pseudopeptide-Based Soft Bioinspired Materials, *New J. Chem.*, 2023, **47**, 20785–20792, DOI: 10.1039/D3NJ04599D.

50 (*a*) A. Tamrakar, P. Kumar, N. Garg, S. V. Luis and M. D. Pandey, Intracellular Zn(II) Induced Turn-on Fluorescence of an l-Phenylalanine-Derived Pseudopeptide, *Org. Biomol. Chem.*, 2023, **21**, 8823–8828, DOI: 10.1039/D3OB01337E; (*b*) A. Tamrakar, S. Asthana, P. Kumar, N. Garg and M. D. Pandey, Design of C_2-symmetric pseudopeptides for in vivo detection of Cu(II) through controlled supramolecular nano-assembly, *Org. Biomol. Chem.*, 2024, **22**, 6409–6418, DOI: 10.1039/D4OB01011F.

51 J. Becerril, M. Bolte, M. I. Burguete, F. Galindo, E. García-España, S. V. Luis and J. F. Miravet, Efficient Macrocyclization of U-Turn Preorganized Peptidomimetics: The Role of Intramolecular H-Bond and Solvophobic Effects, *J. Am. Chem. Soc.*, 2003, **125**, 6677–6686, DOI: 10.1021/ja0284759.

52 S. Yang, H. Kou, H. Wang, K. Cheng and J. Wang, Efficient Electrolyte of N,N′-Bis(Salicylidene)Ethylenediamine Zinc(Ii) Iodide in Dye-Sensitized Solar Cells, *New J. Chem.*, 2010, **34**, 313–317, DOI: 10.1039/B9NJ00405J.

53 E. Faggi, J. Serra-Vinardell, M. D. Pandey, J. Casas, G. Fabriàs, S. V. Luis and I. Alfonso, Pseudopeptidic Fluorescent On-off PH Sensor Based on Pyrene Excimer Emission: Imaging of Acidic Cellular Organelles, *Sens. Actuators, B*, 2016, **234**, 633–640, DOI: 10.1016/j.snb.2016.05.037.

54 D. Maity, S. Kumar Mandal, B. Guha and P. Roy, A Salicylaldehyde Based Dual Chemosensor for Zinc and Arsenate Ion Detection: Biological Application, *Inorg. Chim. Acta*, 2021, **519**, 120258, DOI: 10.1016/j.ica.2021.120258.

55 N. S. Mohamad, N. H. Zakaria, N. Daud, L. L. Tan, G. C. Ta, L. Y. Heng and N. I. Hassan, The Role of 8-Amidoquinoline

Derivatives as Fluorescent Probes for Zinc Ion Determination, *Sensors*, 2021, **21**, 311, DOI: **10.3390/s21010311**.

56 (*a*) T. Wei, J. Wang, Y. Chen and Y. Han, Combining PET and ICT mechanism into one chemosensor for the highly sensitive and selective detection of Zinc, *RSC Adv.*, 2015, **5**, 57141–57146, DOI: **10.1039/C5RA11194C**; (*b*) L. Yan, T. Qing, R. Li, Z. Wang and Z. Qi, Synthesis and optical properties of aggregation-induced emission (AIE) molecules based on the ESIPT mechanism as pH- and Zn^{2+}-responsive fluorescent sensors, *RSC Adv.*, 2016, **6**, 63874–63879, DOI: **10.1039/C6RA09920C**.

57 J. Mou, H. Qi, R. Xiang, S. Xu, J. Liu, S. Meng, N. Chen, Y. Xue and D. Pei, A Novel Fluorescence Sensor for Relay Recognition of Zinc Ions and Nitric Oxide through Fluorescence 'off–on–off' Functionality, *New J. Chem.*, 2021, **45**, 2958–2966, DOI: **10.1039/D0NJ05018K**.

58 (*a*) M. Peng, S. Shi and Y. Zhang, Influence of Cd2+, Hg2+ and Pb2+ on (+)-catechin binding to bovine serum albumin studied by fluorescence spectroscopic methods, *Spectrochim. Acta, Part A*, 2012, **85**(1), 190–197, DOI: **10.1016/j.saa.2011.09.059**; (*b*) M. Anjomshoa, S. J. Fatemi, M. Torkzadeh-Mahani and H. Hadadzadeh, DNA-and BSA-binding studies and anticancer activity against human breast cancer cells (MCF-7) of the zinc (II) complex coordinated by 5, 6-diphenyl-3-(2-pyridyl)-1, 2, 4-triazine, *Spectrochim. Acta, Part A*, 2014, **127**, 511–520, DOI: **10.1016/j.saa.2014.02.048**; (*c*) J. Mao, Y. Zhang, S. Zhang and B. Song, Turn-On Fluorescent Probe for BSA Detection Constructed by Supramolecular Assembly, *Langmuir*, 2024, **40**, 5479–5487, DOI: **10.1021/acs.langmuir.4c00006**.

59 (*a*) R. Singh, N. K. Mishra, N. Singh, P. Rawal, P. Gupta and K. B. Joshi, Transition metal ions induced secondary structural transformation in a hydrophobized short peptide amphiphile, *New J. Chem.*, 2020, **44**, 9255–9263, DOI: **10.1039/D0NJ01501F**; (*b*) H. Chen, X. Cai, J. Cheng and S. Wang, Self-Assembling Peptides: Molecule-Nanostructure-Function and Application on Food Industry, *Trends Food Sci. Technol.*, 2022, **120**, 212–222, DOI: **10.1016/j.tifs.2021.12.027**.

60 K. Kesharwani, R. Singh, N. Kumar, N. Singh, P. Gupta and K. B. Joshi, Mercury-Instructed Assembly (MiA): Architecting Clathrin Triskelion-Inspired Highly Functional C_3-Symmetric Triskelion Nanotorus Functional Structures into Microtorus Structures, *Nanoscale*, 2022, **14**, 10200–10210, DOI: **10.1039/D2NR01524B**.

61 N. Singh, R. Singh, S. Sharma, K. Kesharwani, K. B. Joshi and S. Verma, Transition-Metal Ion-Mediated Morphological Transformation of Pyridine-Based Peptide Nanostructures, *New J. Chem.*, 2021, **45**, 153–161, DOI: **10.1039/D0NJ04260A**.